

Article

# Band Structure Evolution during Reversible Interconversion between Dirac and Standard Fermions in Organic Charge-Transfer Salts

Ryuhei Oka<sup>1</sup>, Keishi Ohara<sup>1,2</sup> , Kensuke Konishi<sup>1,2</sup>, Ichiro Yamane<sup>3</sup>, Toshihiro Shimada<sup>3</sup>   
and Toshio Naito<sup>1,2,4,\*</sup> 

<sup>1</sup> Graduate School of Science and Engineering, Ehime University, Matsuyama 790-8577, Ehime, Japan; okari910@gmail.com (R.O.)

<sup>2</sup> Research Unit for Materials Development for Efficient Utilization and Storage of Energy, Ehime University, Matsuyama 790-8577, Ehime, Japan

<sup>3</sup> Graduate School of Engineering, Hokkaido University, Kita 13, Nishi 8, Kita-ku, Sapporo 060-8628, Hokkaido, Japan

<sup>4</sup> Geodynamics Research Center (GRC), Ehime University, Matsuyama 790-8577, Ehime, Japan

\* Correspondence: tnaito@ehime-u.ac.jp

**Abstract:** Materials containing Dirac fermions (DFs) have been actively researched because they often alter electrical and magnetic properties in an unprecedented manner. Although many studies have suggested the transformation between standard fermions (SFs) and DFs, the non-availability of appropriate samples has prevented the observation of the transformation process. We observed the interconversion process of DFs and SFs using organic charge-transfer (CT) salts. The samples are unique in that the constituents (the donor D and acceptor A species) are particularly close to each other in energy, leading to the temperature- and D-A-combination-sensitive CT interactions in the solid states. The three-dimensional weak D–A CT interactions in low-symmetry crystals induced the continuous reshaping of flat-bottomed bands into Dirac cones with decreasing temperature; this is a characteristic shape of bands that converts the behavior of SFs into that of DFs. Based on the first-principles band structures supported by the observed electronic properties, round-apex-Dirac-cone-like features appear and disappear with temperature variation. These band-structure snapshots are expected to add further detailed understanding to the related research fields.

**Keywords:** organic Dirac electron systems; band structure reshaping; coexistence of standard and Dirac fermions; first-principles band calculation; donor-anion interactions; self-doping



**Citation:** Oka, R.; Ohara, K.; Konishi, K.; Yamane, I.; Shimada, T.; Naito, T. Band Structure Evolution during Reversible Interconversion between Dirac and Standard Fermions in Organic Charge-Transfer Salts. *Magnetochemistry* **2023**, *9*, 153. <https://doi.org/10.3390/magnetochemistry9060153>

Academic Editor: Laura C. J. Pereira

Received: 16 May 2023

Revised: 2 June 2023

Accepted: 5 June 2023

Published: 9 June 2023



**Copyright:** © 2023 by the authors. Licensee MDPI, Basel, Switzerland. This article is an open access article distributed under the terms and conditions of the Creative Commons Attribution (CC BY) license (<https://creativecommons.org/licenses/by/4.0/>).

## 1. Introduction

The physical and chemical properties of common materials are governed by electrons or holes with finite effective masses, i.e., massive fermions [1]. Recently, a series of materials that contain unique particles called Dirac fermions (DFs) have gained considerable scientific attention [1–6]. These particles possess unusually small effective masses and unusually high mobilities because of their Fermi velocities. Owing to these characteristics, the electrons in these materials behave as relativistic massless fermions. DFs regulate the physical properties when located near the Fermi level; these fermions exhibit unique electrical properties such as temperature ( $T$ )-independent resistivity ( $\rho$ ),  $d\rho/dT \sim 0$ . Such behaviors belong to neither metals ( $d\rho/dT > 0$ ) nor nonmetals ( $d\rho/dT < 0$ ). These intriguing physical properties can be attributed to a unique feature that DF systems share in their band structures around the Fermi levels: the band dispersion linearly depends on the wave vectors in the reciprocal space, which leads to cone-shaped bands called Dirac cones [7–32] (Figure 1a). Unlike the unique feature of the band structures of the DF system, the band dispersions in common materials are described by parabolic or cosine bands [1].

A single electron cannot be a DF (massless fermion) and a standard fermion (SF; massive fermion) at the same time. Therefore, the transformation between them, driven by band reshaping, has been focused on in terms of how and why this conversion should occur and how the physical properties should change. Most studies on such transformations are based on theoretical physics [33–44], and the actual transformation, where chemistry also plays an important role, remains elusive.

The organic charge-transfer (CT) salts  $\alpha$ -D<sub>2</sub>I<sub>3</sub> (D = C<sub>10</sub>H<sub>8</sub>S<sub>8</sub> (ET), C<sub>10</sub>H<sub>8</sub>S<sub>6</sub>Se<sub>2</sub> (STF), and C<sub>10</sub>H<sub>8</sub>S<sub>4</sub>Se<sub>4</sub> (BETS); Figure 1b) under ambient pressure are extensively studied, as well as their aspects regarding organic DF systems [19–36,45–62]. However, most studies on them are focused on whether they belong to the zero-gap semiconductors (ZGSs) [19–31,63–66]. It has not been examined experimentally how the reversible conversion of massive and massless fermions occurs in conjunction with the formation of a Dirac-cone-type band. Since the discovery of DFs in graphene and related inorganic substances, many studies have focused on stable two-dimensional (2D) compounds with simple chemical formulae and high structural symmetries [1–16]. Such samples are often more easily available than the organic DF systems and favor clear discussion based on precise theoretical analyses such as first-principles band calculations. Stable inorganic compounds are often obtained as large robust single crystals in large-scale syntheses, whereas few of these conditions are generally observed in organic compounds. However, simple electronic systems rarely exhibit the interconversion between DFs and SFs, as they are thermodynamically too stable and possess lesser degrees of freedom than complicated electronic systems. In this regard, the bulk DF systems in  $\alpha$ -D<sub>2</sub>I<sub>3</sub> exhibited gradual and reversible transformation between DFs and SFs with variation in the temperature *T*, owing to their low-symmetry crystal structures and various weak but non-negligible competing interactions. We demonstrate the validities of the calculated band structures by comparing them with the observed physical properties. Further, we discuss the mechanism of the appearance and disappearance of DFs based on the corresponding band structures. Our finding revealed that the chemical equilibrium in the D-I<sub>3</sub> redox reaction governs the "physical equilibrium" that determines whether the fermions behave as DFs or SFs. Most previous studies on organic DFs have discussed their findings in terms of physics rather than chemistry and focused on the local band structure around the Dirac cones. By providing the whole band structures connected with D-I<sub>3</sub> redox reaction, this study sheds new light on the research on the production mechanism and stability of DFs.

## 2. Materials and Methods

### 2.1. Materials

The single crystals of  $\alpha$ -D<sub>2</sub>I<sub>3</sub> (D = ET, STF, and BETS) and the donor molecules (STF and BETS) were synthesized by following the reported procedures [45–47]. The details of the syntheses are described in Supporting Information (Scheme S1). The neutral ET was purchased from Tokyo Chemical Industry Co., Ltd. (Tokyo, Japan), and used as received. Prior to the physical property measurements, all single crystals were checked by X-ray oscillation photography in terms of their crystal quality and the orientation of crystallographic axes.

### 2.2. Electrical Resistivity Measurements

The electrical resistivities of  $\alpha$ -D<sub>2</sub>I<sub>3</sub> (D = ET, STF, and BETS) were measured by a standard four-probe method using single crystals, gold wires (15  $\mu$ m in diameter, Nilaco), carbon paste, and a physical property measurement system (PPMS-9; 10 mW–5 MW) with EverCool II (Quantum Design). A direct current of 100–200  $\mu$ A was applied depending on the resistivity values. For the resistivity measurement of the insulating phase of  $\alpha$ -ET<sub>2</sub>I<sub>3</sub>, different equipment with a wider dynamic range of resistivity measurement was used (the maximum output = 200 V, resolution = 1 pA) with the same four-probe configuration. The equipment was a home-made cryostat consisting of a digital voltmeter (Keithley Nanovoltmeter 2182A, Tektronics, Tokyo, Japan), a current/voltage source (Keithley SourceMeter 2400, Tokyo, Japan, Tektronics), a digital temperature controller (LakeShore,

Model 331, Lake Shore Cryotronics, Inc., Westerville, OH, USA), and a diffusion/rotary pumping system (DIAVAC, DS-A412N, Diavac Limited, Yachiyo, Japan). To minimize the joule heating of the sample and a resultant thermoelectric power, a constant current ( $\leq 2$  mA) was applied for 20 ms, and the voltage drop was measured in a synchronized way with the current source. Immediately ( $\sim 20$  ms) after the first measurement, the voltage was reversed, and the same measurement was carried out. Then, the average was taken to cancel out the thermoelectric power. At every data acquisition during the resistivity measurement of the insulating phase of  $\alpha$ -ET<sub>2</sub>I<sub>3</sub>, we confirmed that 98–100% values of the set current flew in the sample. In both types of equipment, gold wires (25  $\mu\text{m}\phi$ ) were attached along the *b*-axis on the *ab* planes of the crystals for the electrical contacts. The linearity between current and voltage was checked at every beginning of the measurement at  $\sim 300$  K.

### 2.3. Magnetic Susceptibility Measurements

The magnetic susceptibility was measured using the polycrystalline samples and DC mode of a SQUID susceptometer (Quantum Design MPMS-XL with an EverCool) in both field cooling (FC) and zero-field cooling (ZFC) processes at 2–300 K. The sample was contained in a gelatin capsule with ventilation holes and was set in the middle of a polystyrene straw (Quantum Design); a magnetic field of 1 T was applied. Background signals from the capsule and the straw were independently measured, which were then subtracted from the total susceptibility. The diamagnetic susceptibilities ( $\text{emu mol}^{-1}\text{G}^{-1}$ ) of the ET ( $-2.18 \times 10^{-4}$ ), STF ( $-1.55 \times 10^{-4}$ ), BETS ( $-2.12 \times 10^{-4}$ ), and I<sub>3</sub><sup>−</sup> ( $-3.61 \times 10^{-5}$ ) species were cited from previous studies [26,67,68].

### 2.4. ESR Spectra Measurements

The ESR spectra of the X band (9.3 GHz) were measured using the single crystals of  $\alpha$ -D<sub>2</sub>I<sub>3</sub> in the temperature range of 120–300 K using JEOL JES-FA100 (JEOL Ltd., Tokyo, Japan). The single crystal was mounted on a Teflon piece settled with a minimal amount of Apiezon N grease and sealed in a 5-mm-diameter quartz sample tube in a low-pressure ( $\sim 20$  mm Hg) helium atmosphere. The background signals were measured prior to the sample measurement under conditions identical to those of the samples, and the resultant spectra were subtracted from the raw sample spectra. The *Q*-values, time constant, sweep time, modulation, and its amplitude were 4700–8200, 0.03 s, 1 min, 100 kHz, and 2 mT, respectively. Here, the *Q*-values are the factors indicating the resonance specification of the cavity and are defined as the ratio between the energy stored in the cavity and that consumed inside the cavity. The root dependencies of the ESR intensities on the microwave power were checked (1–10 mW), and the power was selected to be 4 mW or 9 mW depending on the signal intensity. The magnetic field was corrected by a Gauss meter (JEOL NMR Field Meter ES-FC5, Akishima, Tokyo, Japan) at the end of every measurement. The temperature was controlled using a continuous flow-type liquid N<sub>2</sub> cryostat with a digital temperature controller (JEOL). The temperature variation did not exceed  $\pm 0.5$  K during the field sweep. The cooling rate was  $-10$  K/min. No hysteretic behavior was observed in the ESR spectra between the heating and cooling processes.

### 2.5. X-ray Structural Analyses

The single-crystal X-ray structural analyses of  $\alpha$ -ET<sub>2</sub>I<sub>3</sub> (296 K and 100 K) and  $\alpha$ -BETS<sub>2</sub>I<sub>3</sub> (296 K and 100 K) were performed using RIGAKU VariMax SaturnCCD724/ $\alpha$  (graphite monochromated Mo-K $\alpha$  radiation;  $\lambda = 0.71073$  Å) (Rigaku Co., Ltd., Tokyo, Japan) equipped with a nitrogen-gas-flow temperature controller (Cobra, Oxford Cryosystems, Long Hanborough, UK). Regarding the low-temperature measurements, the cooling rate was  $-1$  K/min. The fluctuation in temperature during the data collections was  $\sim \pm 1$  K. The collected data were processed using CrysAlisPro ver. 171.38.46 or ver. 171.41\_64.93a (Rigaku Oxford Diffraction, Tokyo, Japan) prior to the structure determination and refinement using CrystalStructure 4.3.2 (Rigaku Oxford Diffraction, Tokyo, Japan) or Olex 2-1.5 [69]. The

hydrogen atoms on the ethylene groups of the ET and BETS molecules were located at the calculated positions. Further details of the data collection and analyses are described in the .cif files deposited to the Cambridge Crystallographic Data Centre (CCDC). The CCDC deposit numbers of the .cif files are as follows:  $\alpha$ -BETS<sub>2</sub>I<sub>3</sub> 2217842 (100 K) and 2217843 (296 K);  $\alpha$ -ET<sub>2</sub>I<sub>3</sub> 2217847 (100 K) and 2217848 (296 K).

### 2.6. Band Structure Calculation

The electronic band structures of the materials were calculated using the Vienna *Ab initio* Simulation Package (VASP) [70]. PBE functional [71] was used along with the augmented plane wave method. Crystal structures derived from the X-ray diffraction experiments were used, and no structure optimization was performed. The atomic parameters used in the calculation were submitted as cif files. The structural data were partly (80 K and 30 K for  $\alpha$ -BETS<sub>2</sub>I<sub>3</sub> [25] and 150 K and 30 K for  $\alpha$ -ET<sub>2</sub>I<sub>3</sub> [49]) provided by Prof. H. Sawa at Nagoya University in Japan; the remaining structural data (296 K and 100 K for both  $\alpha$ -BETS<sub>2</sub>I<sub>3</sub> and  $\alpha$ -ET<sub>2</sub>I<sub>3</sub>) were obtained in this study as described above. The details of structural analyses were included in the cif files. The energy convergence with the cut-off energy and K-point density was carefully examined and the final cut-off of 1000 eV and  $8 \times 8 \times 4$  K-points were found sufficient to achieve the convergence of the total energy  $< 10^{-3}$  eV/atom.

## 3. Results and Discussion

Below, we briefly summarize the structural and physical properties of  $\alpha$ -D<sub>2</sub>I<sub>3</sub>. These properties are known [19–26,45–50], but are necessary for proving the validity of our calculated band structures. As the observed electronic properties and calculated band structures in previous papers do not always provide necessary information for comparison with our calculated band structures in detail, we re-examined the physical properties shown below. The disorder at the inner-chalcogen (Se and S) atom sites prevented us from evaluating the band structure of  $\alpha$ -STF<sub>2</sub>I<sub>3</sub> using the same calculation as that employed for the other two salts [21,26,63]. Thus, we will not discuss the band structure of  $\alpha$ -STF<sub>2</sub>I<sub>3</sub> and will only discuss the physical properties of  $\alpha$ -STF<sub>2</sub>I<sub>3</sub> for comparison. There are papers showing that the STF salt belongs to the ZGSs at ambient pressure despite the disorder at the STF sites [21,26,36,63]. Thus, the physical properties of  $\alpha$ -STF<sub>2</sub>I<sub>3</sub> augment the current understanding of the behavior of the DFs in  $\alpha$ -D<sub>2</sub>I<sub>3</sub>.

### 3.1. Crystal Structures of $\alpha$ -D<sub>2</sub>I<sub>3</sub>

Except for the change in the space group in the phase transition at 135 K for  $\alpha$ -ET<sub>2</sub>I<sub>3</sub>, the crystal structures of  $\alpha$ -D<sub>2</sub>I<sub>3</sub> (D = ET, STF, and BETS; Figure 1c,d) are qualitatively identical and practically independent of the temperature *T*, which is consistent with that reported in the previous studies [19,45–49]. An important feature is that there are weak and *T*-dependent charge-transfer (CT) interactions between D and I<sub>3</sub> in addition to the strong D–D CT interactions that yield D<sup>(0.5– $\delta$ /2)+</sup> and I<sub>3</sub><sup>(1– $\delta$ )–</sup> ( $0 < \delta \ll 1$ ) [72,73]; this indicates that both D and I<sub>3</sub> are radical species. The band formation is dominated by D–D interactions, whereas band reshaping is driven by D–I<sub>3</sub> interactions [72,73]. The D cations aggregate via S–S short (<van der Waals distance of 3.70 Å) contacts, and they form 2D conduction sheets in the *ab* planes. In addition, the I<sub>3</sub> anions are sandwiched between these sheets, and they develop H bonds with the ethylene groups of the D cations (C–H–I). The D–I<sub>3</sub> interactions occur via different pathways based on the C–H–I contacts (H–I distances of *ca.* 3.0–3.5 Å). The amount of CT between D and I<sub>3</sub> depends on *T*. This structural feature produces rather complicated hyperfine structures in the electron spin resonance (ESR) spectra, as discussed hereinafter, which provides evidence for the D–I<sub>3</sub> interactions.

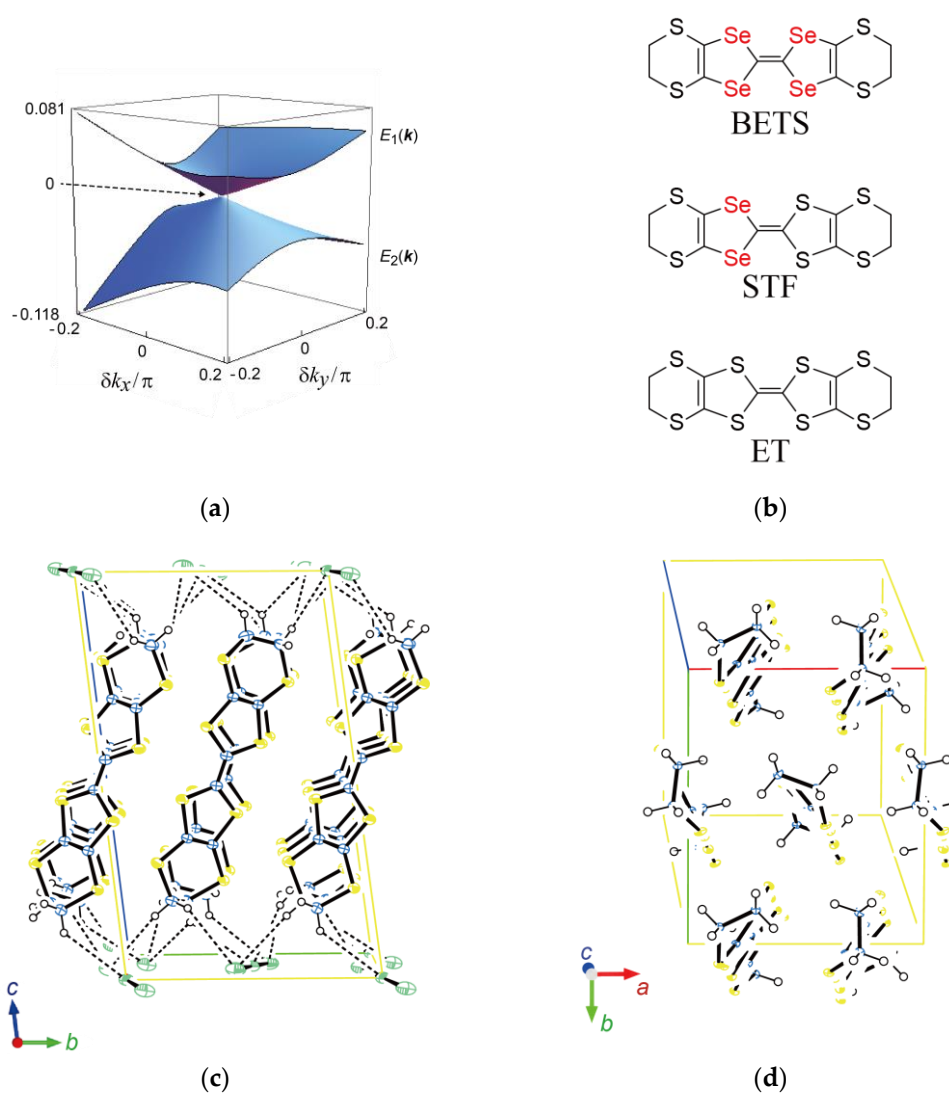


**Figure 1.** Organic Dirac fermion systems: (a) A characteristic band structure of Dirac fermion (DF) systems in the zero-gap semiconductors around a Dirac point, which is the apex of the cone indicated by a broken arrow. In this example, a pair of bands ( $E_1(k)$  and  $E_2(k)$ ) form a cone-type band structure in the  $k_x k_y$  space. © 2020 The Physical Society of Japan (J. Phys. Soc. Jpn. 89, 023701) [21]; (b) Chemical structures of ET = bis(ethylenedithio)tetrathiafulvalene, STF = bis(ethylenedithio)diselenadithiafulvalene, and BETS = bis(ethylenedithio)tetraselenafulvalene; (c) Crystal structures (view along the  $a$  axis) of  $\alpha$ -ET<sub>2</sub>I<sub>3</sub>. The broken lines represent (C)-H---I and (C)-H---S contacts that are shorter than the van der Waals distances, i.e., 3.35 and 3.05 Å, respectively. These contacts demonstrate the ET–I<sub>3</sub> interactions, which drive band reshaping and transformation between SFs and DFs; (d) Crystal structures (view along the  $c$  axis) of  $\alpha$ -ET<sub>2</sub>I<sub>3</sub>. The I atoms are omitted in Figure 1d for clarity.

### 3.2. Physical Properties of $\alpha$ -D<sub>2</sub>I<sub>3</sub>

Figure 2 shows the  $T$  dependencies of the electrical resistivity ( $\rho$ : Figure 2a,b) and paramagnetic susceptibility ( $\chi_p$ : Figure 2c,d) of  $\alpha$ -D<sub>2</sub>I<sub>3</sub>. Below  $\sim 120$  K, the resistivity of  $\alpha$ -ET<sub>2</sub>I<sub>3</sub> exhibited a very small temperature dependence (activation energy  $\sim 5.2$  meV at 78–105 K). This activation energy well agreed with the present band calculation (4.23 meV at 100 K) as discussed below. Additionally, our observation of the temperature-dependent activation energy, which clearly decreased at  $\sim 70$  K, agrees quantitatively with the previous study [74]. The paramagnetic susceptibility  $\chi_p$  manifests the net contribution of the carriers to the magnetic susceptibility. The high values of  $\chi_p$  below 135 K appears to contradict the

fact that this salt is in the insulating phase below 135 K. However, a substantial number of residual spins were observed in the insulating phase of  $\alpha$ -ET<sub>2</sub>I<sub>3</sub>.

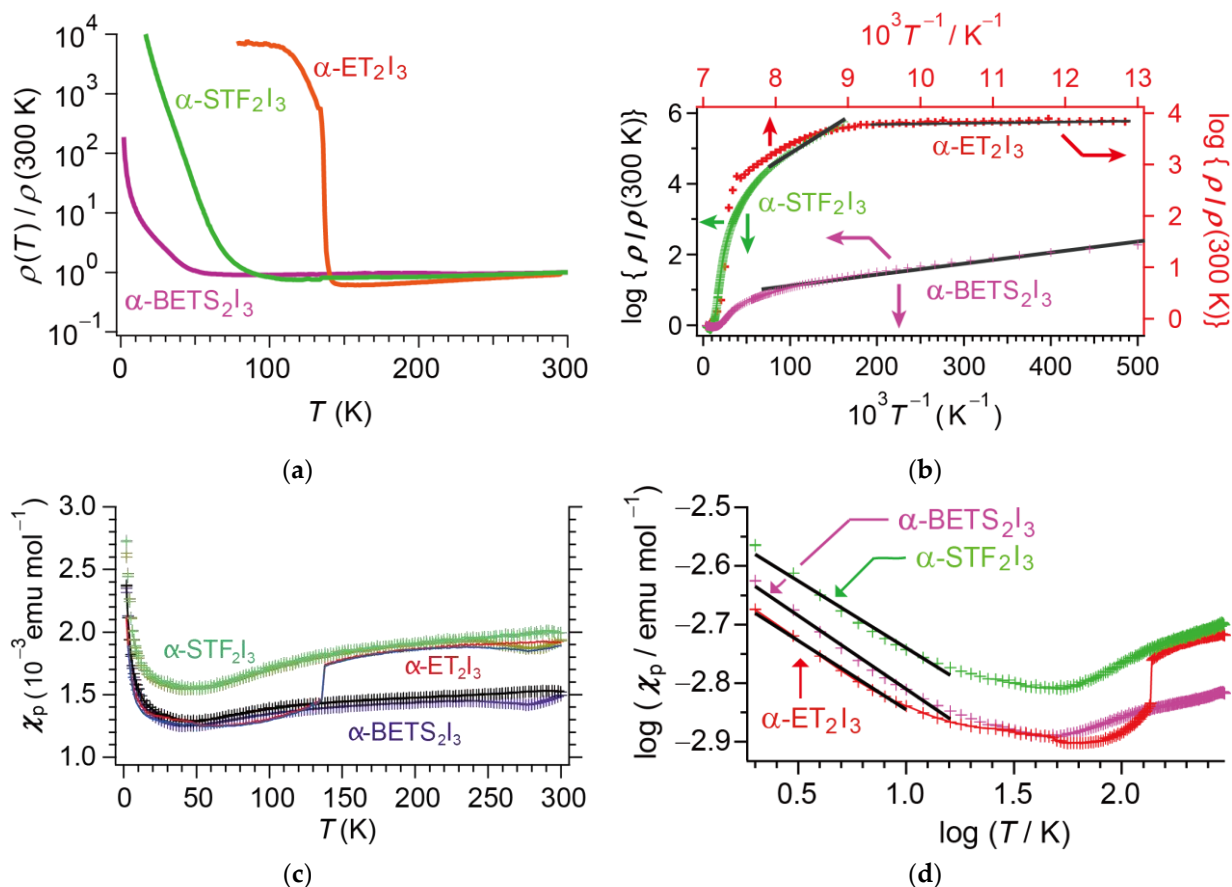


**Figure 2.** Temperature ( $T$ ) dependencies of the physical properties ( $\rho$ ) of  $\alpha$ -D<sub>2</sub>I<sub>3</sub>: (a) Electrical resistivity ( $\rho$ ). D = ET (red), STF (green), and BETS (violet). The vertical axis for  $\rho$  is normalized by  $\rho$  at 300 K. The absolute values of  $\rho$  at 300 K for the three materials are 47 (D = ET), 2.2 (D = STF), and 2.9 (D = BETS) in the unit of  $10^{-2} \Omega \text{ cm}$ ; (b) Enlarged view of  $\rho$  at low  $T$ , which shows thermally activated  $T$ -dependence near the ground states. Energy gaps estimated from the best-fit lines are 5.2 (ET, 78–105 K), 6.7 (STF,  $T \leq 16$  K), and 1.4 (BETS,  $T \leq 16$  K) meV; (c) Paramagnetic susceptibility ( $\chi_p$ ). D = ET (red = field-cooling (FC) and blue = zero-field cooling (ZFC)), STF (green = FC and pale brown = ZFC), and BETS (black = FC and violet = ZFC). The absolute values of  $\chi_p$  at 300 K for the three materials are 1.9 (D = ET), 2.0 (D = STF), and 1.5 (D = BETS) in the unit of  $10^{-3} \text{ emu G}^{-1} \text{ mol}^{-1}$ ; (d) Enlarged view of  $\chi_p$  at low  $T$ , which shows a unique power-law  $T$ -dependence near the ground states. The  $T$ -dependencies of  $\chi_p$  near the ground states are different from those of  $\rho$  in each  $\alpha$ -D<sub>2</sub>I<sub>3</sub>. D = ET (red), STF (green), and BETS (violet). Black lines represent the best-fit lines in the indicated  $T$  ranges:  $\chi_p \propto T^{-0.24}$  ( $T < 10$  K),  $\chi_p \propto T^{-0.23}$  ( $T < 16$  K), and  $\chi_p \propto T^{-0.25}$  ( $T < 16$  K) for D = ET, STF, and BETS, respectively.

For example, Venturini et al. [53] and Sugano et al. [54] measured the ESR of the single crystals of  $\alpha$ -ET<sub>2</sub>I<sub>3</sub> down to 76 K and 5 K, respectively. Uji et al. measured the resistances in the  $ab$  plane at low-bias voltages of  $\alpha$ -ET<sub>2</sub>I<sub>3</sub> down to  $\sim 30$  K [55]. These studies indicate the existence of (thermally excited) unpaired electrons/holes well below 135 K. Both  $\rho$  and  $\chi_p$  exhibit a metal–insulator (M–I) transition at 135 K for  $\alpha$ -ET<sub>2</sub>I<sub>3</sub> (Figure 2a,c); the metallic carriers (SFs) disappear below this temperature [48,50]. The values of  $\chi_p$  and  $\rho$  at  $T < 135$  K are considerably high and low, respectively, for the insulating solids, which suggests that there is a different type of carriers (fermions) that dominates  $\chi_p$  and  $\rho$  at  $\sim 100 \leq T < 135$  K. The calculated band structure (Figure 3) indicates that the carriers contain thermally excited holes and electrons across the band gaps of a few millielectronvolts at the Dirac points.

Depending on the chemical potential varying with  $T$ , these carriers should behave as DFs when they are thermally excited and are located at the linear band curvatures of the Dirac cones. At  $T \leq 30$  K, the thermally excited carriers are massive (SFs) because there are no more Dirac cones in the bands. The complicated  $T$  dependencies of the band structures (Figure 3, Supplementary Figure S1) create a striking contrast with the monotonical  $T$  dependencies of the electrical and magnetic properties of  $\alpha$ -D<sub>2</sub>I<sub>3</sub> (Figure 2) except for the M–I transition of  $\alpha$ -ET<sub>2</sub>I<sub>3</sub>. This is because SFs and DFs coexist to contribute to the physical properties in a wide  $T$  range; the ratio (SFs/DFs) varies sensitively with  $T$ . The coexistence of SFs and DFs in some materials was previously suggested for  $\alpha$ -ET<sub>2</sub>I<sub>3</sub> [28,64,65] and was reviewed for other materials [75]. Therefore, we cannot explain all physical properties from room temperature to the ground states based exclusively on either SFs or DFs in  $\alpha$ -D<sub>2</sub>I<sub>3</sub>. Similar cases are reported in different types of materials: the physical properties of some DF systems can be understood by assuming that they contain different types of fermions [26,76–78]. The importance of electronic correlation effects on the physical properties of  $\alpha$ -ET<sub>2</sub>I<sub>3</sub> is also discussed [19,28,29].

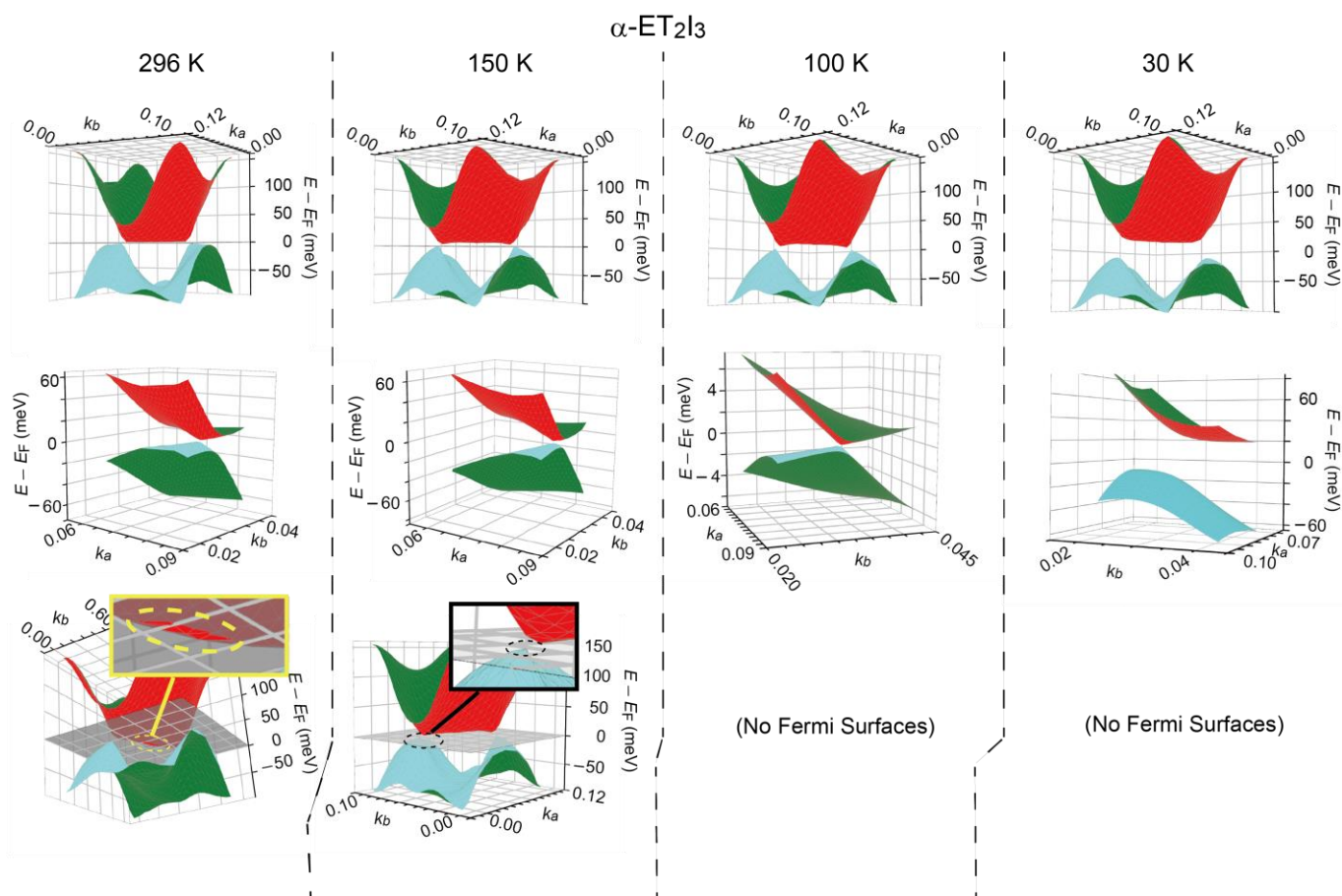


**Figure 3.**  $T$ -dependent band structures for  $\alpha$ -ET<sub>2</sub>I<sub>3</sub>. The figures in the middle row from the left to the right show the gradual growth of Dirac cones from the flat-bottomed bands with decreasing  $T$  followed by the disappearance of the Dirac cones at 30 K. The Fermi levels ( $E_F$ ) are indicated by the gray plane in the bottom figures (296 and 150 K). (Top) The outline, (middle) close-up views of the calculated band structures at the Dirac points, and (bottom) close-up views of the calculated band structures on the Fermi surfaces. The broken ovals in the bottom figures indicate the locations where  $E_F$  intersects the bottom of the top (red) band (296 K) or the top of the bottom (blue) band (150 K). The band gap between the Dirac cones at 100 K in the figure appears significantly smaller than the actual band gap (4.23 meV) because the viewing angle is highly inclined against the vertical (energy) axis.

### 3.3. Calculated Band Structures of $\alpha$ -ET<sub>2</sub>I<sub>3</sub>

The accuracy of the present band calculation is demonstrated to be  $\sim 0.04$  meV by a series of closely related calculations of different groups [64,79,80]. Initially, the acquired band structures of  $\alpha$ -ET<sub>2</sub>I<sub>3</sub> (Figure 3) are discussed by comparing them with the observed physical properties of  $\alpha$ -ET<sub>2</sub>I<sub>3</sub> (Figure 2) to confirm the validity of the band calculation. The closely related band structures of  $\alpha$ -BETS<sub>2</sub>I<sub>3</sub> (Figure 4) and physical properties of the remaining  $\alpha$ -D<sub>2</sub>I<sub>3</sub> (D = STF and BETS) are described in this section to demonstrate the general aspects of band reshaping associated with the physical properties. Figure 3 depicts the band structures of  $\alpha$ -ET<sub>2</sub>I<sub>3</sub> calculated using the Vienna *ab initio* simulation package based on the crystal structures at 296, 150, 100, and 30 K under ambient pressure. We initially discuss the band structures obtained in the metallic phase (296 and 150 K) followed by those acquired in the insulating phase (100 and 30 K) because  $\alpha$ -ET<sub>2</sub>I<sub>3</sub> demonstrates an M–I transition at 135 K, where drastic changes in the band structures and physical properties are expected [48–50].

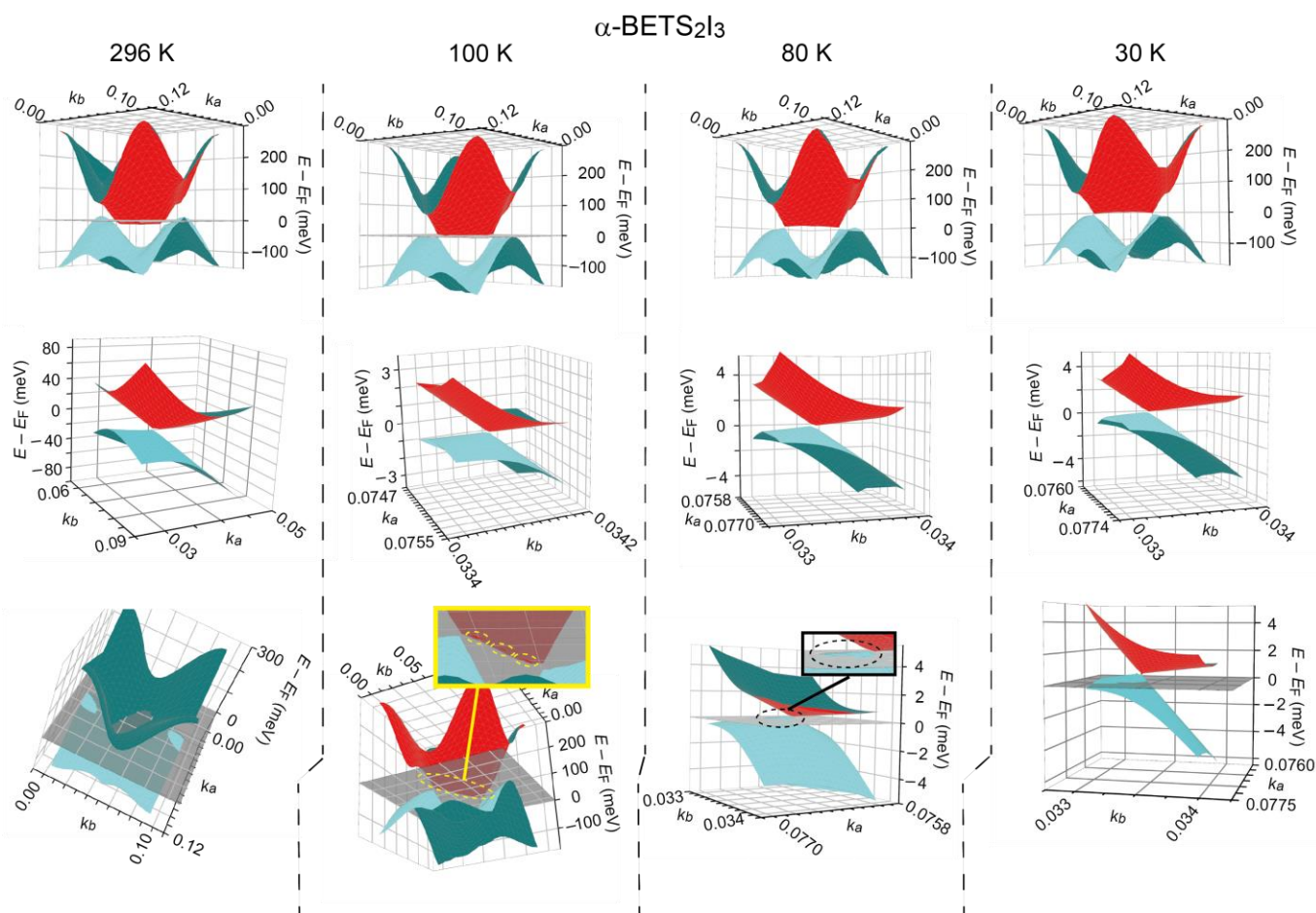


**Figure 4.** *T*-dependent band structures for  $\alpha$ -BETS<sub>2</sub>I<sub>3</sub>. The figures in the middle row from the left to the right show the gradual changes in band filling and band shape with decreasing *T*. The Fermi levels ( $E_F$ ) are indicated by the gray plane in the bottom figures. (Top) The outline, (middle) close-up views of the calculated band structures at the Dirac points, and (bottom) close-up views of the calculated band structures on the Fermi surfaces. The yellow and black broken ovals in the bottom figures represent the Fermi surfaces at 100 and 80 K, respectively.

$\alpha$ -ET<sub>2</sub>I<sub>3</sub> exhibits the characteristic 2D ET arrangement and isotropic metallic conduction in the *ab* plane at 296 K. The obtained band structure at 296 K indicates significantly isotropic metallic dispersion in the  $k_a k_b$  plane, and it is qualitatively consistent with the crystal structure and conducting properties. Furthermore, the acquired band structures

have two important features in terms of band reshaping, which are driven by the ET-I<sub>3</sub> CT interactions.

First, the Fermi level is located at the top bands (red) of the four highest occupied molecular orbitals (HOMOs) of ET and the second band (blue) is fully filled. This implies that ET cation radicals are not quarter-filled (ET<sup>+0.5</sup> and I<sub>3</sub><sup>-</sup>) but are electron doped by the I<sub>3</sub> anions (ET<sup>(0.5-d/2)+</sup> and I<sub>3</sub><sup>(1-d)-</sup>). This contradicts the early-stage band calculation finding of a semi-metallic band structure with almost-equal areas of electron and hole pockets [51], where they did not consider ET-I<sub>3</sub> interactions. In most of the previous band calculations, some did not consider the CT interaction between I<sub>3</sub> and D [25,51,60,61,64,66], while some included the I<sub>3</sub> anions but obtained band structures with a negligible effect of the I<sub>3</sub>-D CT interactions [24,62]. As a result, many of them suffered from some inconsistency with the observed physical properties or adjusted some parameters such as spin-orbit coupling constants to agree with the observations. The present band structure contains both electrons and holes as thermally excited Dirac electrons and holes, in addition to the normal electrons at the Fermi surface. Additionally, the calculated band gap between the Dirac cones is less than a few meV (~5–50 K) depending on the temperature  $T$ , implying that there are thermally excited Dirac electrons and holes as a part of the carriers down to the lowest  $T$  of the measurements in this work (~2 K). Their contribution to physical properties depends not only on their numbers but also on their mobilities and anisotropies. Thus, we cannot tell whether such a type of material would behave as a hole or electron conductor solely from the calculated band structures. The  $T$ -sensitive band structures make the major carriers' sign more unpredictable. This feature of band structure is common for  $\alpha$ -D<sub>2</sub>I<sub>3</sub> (D = ET (Figure 3), BETS (Figure 4)). The validity of these bands should be confirmed by the data of Hall coefficients and thermoelectric power for  $\alpha$ -ET<sub>2</sub>I<sub>3</sub> at 1 bar and  $T \geq 30$  K; yet, they are not reported. For  $\alpha$ -BETS<sub>2</sub>I<sub>3</sub> at 1 bar, only the Hall coefficients are reported, which are small and noisy at  $T \geq 50$  K [81]. The observed change in the sign of Hall coefficients of  $\alpha$ -BETS<sub>2</sub>I<sub>3</sub> at ~150 K can be partly explained by the present band calculation indicating that either holes or electrons are doped from I<sub>3</sub> to BETS depending on  $T$  (Figure 4). Therefore, our calculation does not contradict with previous experimental results. The bottom of the top band is apparently flat, and it produces a small Fermi surface as a shallow electron pocket at approximately  $(k_a, k_b) = (0.05, 0.05)$ . The nonlinear band curvature around the Fermi surface renders the doped electrons to behave as SFs. Dirac cones can barely be recognized because of the flattening of the bottom band.

The second feature is a small indirect bandgap at the Dirac point  $E_g(296 \text{ K}) = 2.91 \text{ meV}$ . The band structure at 296 K is metallic with a Fermi surface at approximately  $(k_a, k_b) = (0.05, 0.05)$ ; however, an energy gap exists between two Dirac points at approximately  $(k_a, k_b) = (0.025, 0.06)$  and  $(0.08, 0.035)$ . The developing Dirac points are situated at substantially different positions from the Fermi surfaces, which supports the theory that massless (Dirac) and massive (standard) fermions can coexist. Below 150 K, a further decrease in  $T$  causes the curvatures of the band structures to gradually transform around the Fermi level. The nearly flat-bottomed top (red) band along with the second (blue) band at 296 K starts to develop a Dirac-cone-like shape at 150–100 K. Indirect band gaps between “primitive Dirac points”, i.e., the lowest and highest energy points in the top and second bands, respectively, were 3.71 meV at 150 K and 4.23 meV at 100 K. This allows the coexistence of DFs and SFs, and is quantitatively consistent with the observed electrical, magnetic, and optical properties.

At 100 K, the small Fermi surface located at the bottom of the top band at 296 K disappears, which results in an insulating band structure consistent with the observation of the electrical and magnetic properties (Figure 2). The band gap ( $E_g(100 \text{ K}) = 4.23 \text{ meV}$ ) is indirect and located around the Dirac points. Although the Dirac cones are unclear, band dispersion around both ends of the top bands show linear curvatures, which render the electrons (and holes) massless (DFs). Similarly, thermal excitation across the band gap between “primitive Dirac points” produces Dirac-like electrons and holes, which account for the observed high electrical conductivity in the insulating phase ( $T < 135 \text{ K}$ ). The activation energy at 78–105 K (5.2 meV), derived from the  $T$ -dependent  $\rho$  (Figure 2b),

quantitatively agreed with our calculated band gap (4.23 meV at 100 K). There is a theoretical paper suggesting the essential change in Dirac cones at  $\sim 100$  K, in addition to the coexistence of the standard and Dirac fermions depending on the temperature [64]. Despite the sharp M–I transition at 135 K, the band structure, which includes the band gap, almost retained its shape between metallic (150 K) and insulating (100 K) phases. The curvature of the top band slightly changed from convex (296 K) to concave (100 K). The electrons accommodated in the top band at 296 K completely disappeared at 100 K, which led to the disappearance of the Fermi surface. Unlike common M–I transitions, the transition in  $\alpha$ -ET<sub>2</sub>I<sub>3</sub> does not originate from band splitting with the loss of all unpaired electrons or holes; instead, it originates from the band reshaping associated with the ET–I<sub>3</sub> CT interactions. As a CT interaction is a kind of redox reaction, the degree of CT interactions depends on  $T$ , and affects details of the band structures and band fillings (the number of carriers) simultaneously. This scenario of band reshaping across the M–I transition is consistent with that discussed in previous studies [49,52–55]. Such a  $T$ -sensitive band structure results in the coexistence and reversible interconversion between DFs and SFs. A previous optical study on  $\alpha$ -ET<sub>2</sub>I<sub>3</sub> at 17 K revealed that the energy gap in the insulating phase was 75 meV [52]. This optically estimated value should be compared with the corresponding energy difference in our calculation, namely,  $\sim 85$  meV, because this value corresponds to a direct gap around the location of the Fermi surface in the metallic band structure, which agrees with the optically observed value (75 meV).

At 30 K, the bottom of the top band became nearly flat again, and the band gap ( $\sim 26.8$  meV) became evident at the Fermi level, which completed the M–I transition. This band reshaping can be referred to as merging; that is, a pair of symmetry-related Dirac cones merge into a flat-bottomed band, which simultaneously lose Dirac points, Dirac cones, and DFs.

The calculated band structures of  $\alpha$ -BETS<sub>2</sub>I<sub>3</sub> at 296 K, 100 K, 80 K, and 30 K are shown in Figure 4. At 296 K, both top (red) and second (blue) BETS HOMO bands intersect with the Fermi level, indicating that  $\alpha$ -BETS<sub>2</sub>I<sub>3</sub> at 296 K belongs to a semimetal. This is consistent with the observed behavior of electrical resistivity and magnetic susceptibility (Figure 2). Notably, the bottom of the top (red) band remains rather flat at all the temperatures, suggestive of merging between two overtilted Dirac cones [23,25,33–35,81]. Both top and second HOMO bands in the BETS salt possess about twice widths of those of corresponding bands in the ET salt, reflecting stronger D–D interactions in the BETS salt than those in the ET salt. There are band gaps between primitive Dirac points, namely 2.60 meV (296 K), 0.014 meV (100 K), 1.28 meV (80 K), and  $-0.04$  meV (30 K). Herein, the negative sign of the band gap at 30 K implies that the energy of the bottom of the top-band Dirac cone is higher than that of the top of the second-band Dirac cone. The calculated band gaps strongly agree with previously reported values [25,81]. All these band-structure features indicate the BETS salt is close to overtilting and the merging of a pair of Dirac cones, as well as close to a ZGS at ambient pressure in the ground state as previously suggested by calculations [24,25]. Regarding the band reshaping, Figures 3 and 4 show that  $\alpha$ -D<sub>2</sub>I<sub>3</sub> (D = ET and BETS) share a qualitative  $T$ -dependence. In our calculation,  $\alpha$ -BETS<sub>2</sub>I<sub>3</sub> retained the metallic band structure down to 30 K. However, the electrical resistivity of  $\alpha$ -BETS<sub>2</sub>I<sub>3</sub> smoothly commenced to increase at  $\sim 50$  K (Figure 2a), while the magnetic susceptibility took the broad minimum at  $\sim 30$  K (Figure 2c). These observed electronic behaviors suggest the significant effects of fluctuation and/or strong electron correlation at low  $T$  in  $\alpha$ -BETS<sub>2</sub>I<sub>3</sub> [22]. The calculated band structures would be inconsistent with the observed electronic properties owing to fluctuation and/or strong electron correlation, because they were not considered in the calculation.

In previous work, the reflectance spectra clearly exhibited Drude-type dispersions at 300–25 K for  $\alpha$ -BETS<sub>2</sub>I<sub>3</sub> and  $\alpha$ -STF<sub>2</sub>I<sub>3</sub>, indicating that both salts should be metallic without M–I transitions ( $T \geq 25$  K) [26,46]. Meanwhile, for both salts, the electrical resistivities and magnetic susceptibilities began to increase at  $T_0 \sim 50$  K (BETS) and  $T_0 \sim 80$  K (STF) with decreasing temperature toward the ground states (Figure 2), suggesting that their ground states should be non-metallic. In both STF and BETS salts, if we assume an M–I

transition from a semimetal with a flat-bottomed band at  $E_F$  and almost-vanishing Fermi surfaces to a band insulator with a band gap of the order of  $1 \text{ meV} = 8 \text{ cm}^{-1}$ , the reflectance spectra ( $450 \text{ cm}^{-1}$ – $25,000 \text{ cm}^{-1}$  at  $25$ – $300 \text{ K}$ ) cannot be distinguished from those of metallic materials. Accordingly, the M-I transition and the metallic reflectance spectra can be reconciled with each other based on the present band calculation.

The obscure M-I transitions in the  $\rho$  and  $\chi$  in the BETS and STF salts are explained by continuous band and Fermi surface deformations with temperature variation. With decreasing temperature across the transition, the effects of continuous shrinking (and finally disappearance) of Fermi surfaces make the M-I transition obscure, as observed in the electrical and magnetic properties of the BETS and STF salts. In fact, their unit cell volumes did not exhibit any discontinuous change at  $30$ – $300 \text{ K}$  [25,26]. Accordingly, the M-I transitions should be of second or higher order for both STF and BETS salts. Furthermore, the M-I phase transition model proposed here accounts for the observed non-Arrhenius behavior immediately below  $T_0$  (STF and BETS) or  $T_{MI}$  (ET) in all  $\alpha$ - $D_2I_3$  regarding both of  $\rho$  vs.  $T$  and  $\chi$  vs.  $T$  (Figure 2).

A unique chemistry underlies the abovementioned reshaping of band structures in  $\alpha$ - $ET_2I_3$  and  $\alpha$ - $BETS_2I_3$ . We will discuss this problem more in detail in Section 3.5. The D- $I_3$  interactions has three kinds of effects. Namely, they produce a small number of carriers in the D-main bands, they make the conduction system weakly three-dimensional, and they weaken the D-D interactions in exchange for adding the D- $I_3$  interactions. To lower the energy of such a small carrier system, shallow convex curvature in the band around the Fermi level would be effective to accommodate the electrons at the bottoms of the downward convex curvature, whether such curvature is a shallow hollow at the bottom of the band at the Fermi level (SFs) or a pair of shallow round-apex cones (DFs). In  $\alpha$ - $D_2I_3$  ( $D = ET, BETS$ ), such slight band structure reshaping would be realized only by changes in a part of the electron distribution without the cost of lattice deformation. This is one of the possible mechanisms to explain the  $T$ -sensitive band structure. If they had many carriers at the Fermi level in a wide band with a higher anisotropy, and if the D- $I_3$  interactions were negligible, the metal-insulator transition would involve band splitting with an evident crystal structure change in the D arrangement.

### 3.4. Spectroscopic Evidence for the Occurrence of DFs: ESR

Figure 5 shows the  $T$  dependencies of the ESR spectra of the ET salt under ambient pressure. The direction of the magnetic field  $B$  was parallel ( $0^\circ$ ,  $B // a$ -axes) or perpendicular ( $90^\circ$ ) to the main conduction sheets ( $ab$  planes). Even during the M-I transition, the  $T$  dependence was hardly observed in either the  $0^\circ$  or the  $90^\circ$  spectra. Instead, a significant angular dependence was noticed between the  $0^\circ$  and  $90^\circ$  spectra for the peaks centered at  $\sim 328 \text{ mT}$  ( $g = 2.006$ ); they were assigned to the carriers based on the following discussion. First, we discuss the  $T$  dependencies of these peaks in both spectra. If these peaks originate from metallic carriers, i.e., massive fermions, they should disappear below  $135 \text{ K}$ , because the salt is an insulator below  $135 \text{ K}$ . However, this is not the case here: we still observed ESR signals below  $135 \text{ K}$ . As stated above, a substantial number of spins were observed below  $135 \text{ K}$  in different physical properties of  $\alpha$ - $ET_2I_3$  in previous studies [53–55]. The ESR signal intensity is not simply proportional to the number of spins when the signal originates from different kinds of spin systems with different relaxation times. The signal intensities from the different spin systems may exhibit different anisotropies, which would also deviate the  $T$ -dependence of the intensity from what is anticipated based on the number ratio between each type of spin. In this case, (Figure 5), the signal (line shape) changed from a Dysonian type (asymmetric, characteristic to metals) to a Lorentzian type (symmetric, characteristic to insulators) at the phase transition as shown in Figure 5c, which is consistent with previous work [53,54,82]. Therefore, the ESR results reconcile with the metal-insulator transition. The observation of spins in the insulating phase is explained by assuming that there are two types of carriers, i.e., metallic carriers (massive fermions) and thermally excited Dirac (massless) fermions (Figure 6), and that only the metallic carriers disappear below  $135 \text{ K}$ .

Yet, a substantial number of the carriers remain by fluctuation of metal–insulator transition and thermal excitation. This assumption is consistent with the substantially high  $\chi_p$  and low  $\rho$  of the “insulating” phase (Figure 2).

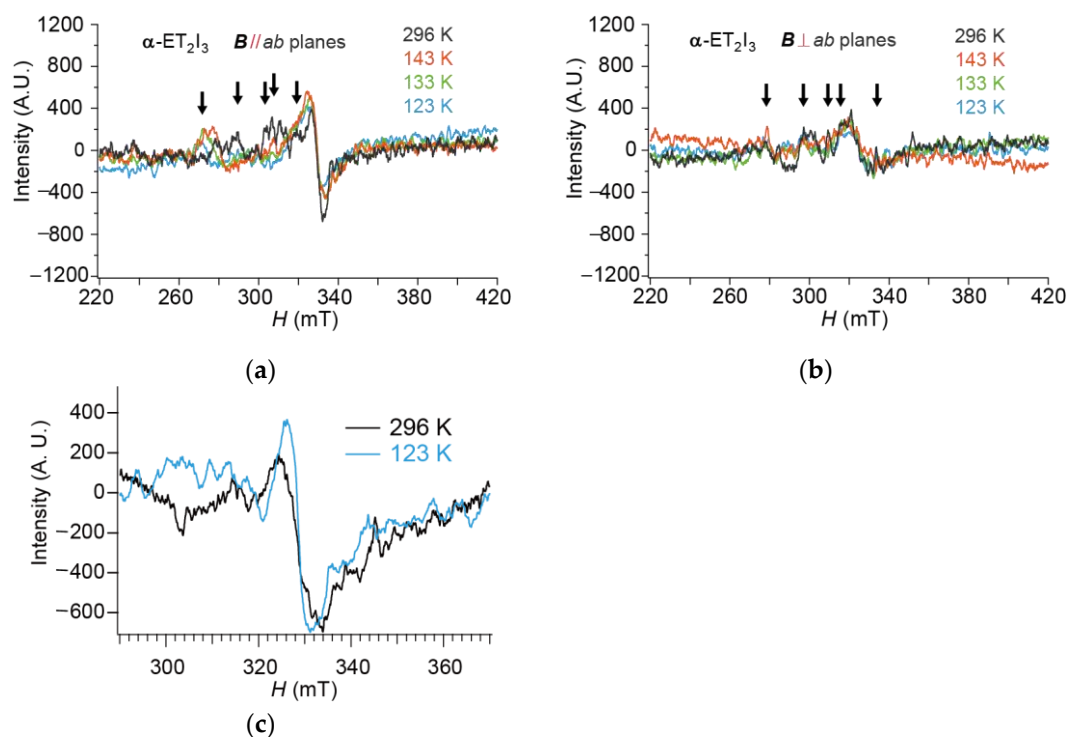


**Figure 5.**  $T$ -dependent ESR spectra of  $\alpha$ - $\text{ET}_2\text{I}_3$ : (a)  $0^\circ$  spectra; (b)  $90^\circ$  spectra; and (c) enlarged view for comparison of the line shapes between metallic (296 K) and insulating (123 K) phases. The 123 K spectrum is vertically offset for easy comparison of the height/depth of the peaks/valleys. The spectra in a and b were obtained from the same single crystal. The spectra in c were obtained from the different sample from those in a and b to show the reproducibility of the Dysonian (296 K) and Lorentzian (123 K) line shapes. The black arrows indicate possible hyperfine (nuclear spin–electron spin) or superhyperfine (nuclear spin–nuclear spin) structures.

The evidently weaker intensities of the peaks at all measured  $T$  in the  $90^\circ$  spectra compared to those in the case of the  $0^\circ$  spectra are noteworthy because they indicate the occurrence of DFs. The difference is prominent only around the peak at  $\sim 328$  mT. This observation is contrary to the general observation in the ESR spectra of 2D organic conductors that contain only SFs [82]. The application of  $B$  in the  $90^\circ$  direction generally yields a stronger peak than that when  $B$  is applied in the  $0^\circ$  direction [82]. However, the thermally excited DFs in  $\alpha$ - $\text{ET}_2\text{I}_3$  at 1 bar contribute significantly to electrical conduction in the  $ab$  plane, and they generate only weak ESR signals because of their short relaxation times originating from their unusually large Fermi velocities.

Based on the calculated band structures, this finding can be explained by the peak at  $\sim 328$  mT being associated with both SFs and DFs (Figure 5). Both fermions are unpaired electrons and holes, and some are produced by thermal excitation depending on the temperature. The contributions of these carriers to the ESR signal continuously crossover with a variation in  $T$ . Thermally excited DFs are important below the M–I transition  $T$  (135 K). Accordingly, at  $T = \sim 100$ – $135$  K, the weak signal at  $\sim 328$  mT in the  $90^\circ$  spectra is associated with the dominant roles of thermally excited DF in the electrical and magnetic properties of  $\alpha$ - $\text{ET}_2\text{I}_3$  in the  $ab$  planes.

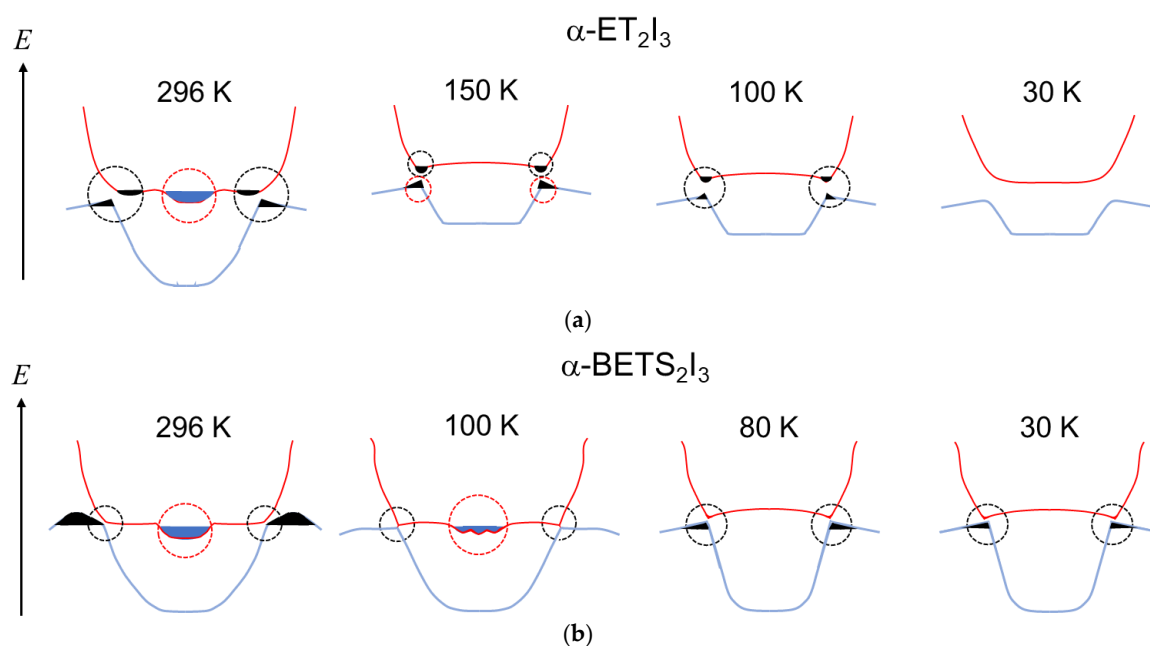
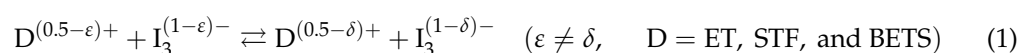


**Figure 6.** Schematic  $T$ -driven band reshaping of: (a)  $\alpha$ - $\text{ET}_2\text{I}_3$ ; and (b)  $\alpha$ - $\text{BETS}_2\text{I}_3$ . From left to right, the figures show small but qualitative changes in the band structure and band filling of the electrons and holes with decreasing  $T$ . Red and blue curves represent the top and second HOMO bands, respectively. For the ET salt, at 296, 150, and 100 K, the shaded areas in the black broken circles at the growing Dirac points indicate thermally excited electrons (in the top band) and holes (in the second band), both of which are Dirac fermions (massless). For the ET salt, at 296 and 150 K, the shaded areas in the red broken circles represent the metallic carriers on the Fermi surface (massive fermions at 296 K and massless fermions at 150 K). Similarly, for the BETS salt, the shaded areas in the black (at 296, 80, and 30 K) and red (at 296 and 100 K) broken circles at the Dirac points indicate metallic carriers (black = filled with holes, blue = filled with electrons) on the Fermi surfaces. For the BETS salts, thermally excited electrons/holes at the Dirac points are not drawn, for they may be confused with the metallic carriers at the Dirac points. In the case of the BETS salt at 100 K, the Dirac points are slightly lower than the Fermi level in energy.

Complicated structures are noticed at  $\sim 220$ – $420$  mT in both  $0^\circ$  and  $90^\circ$  spectra at all  $T$ . As the spins on the I atoms ( $I = 5/2$ ) in the  $\text{I}_3$  anions exhibited hyperfine or superhyperfine structures, some structures were intrinsic. In fact, they partially demonstrated consistent and reproducible responses to different microwave powers (Supplementary Figure S1) and different samples/independent measurements. The observed microwave power dependencies of the peaks are quantitatively explained by hypothesizing three types of spin systems with different saturation behaviors (for details, see the note in the caption of Supplementary Figure S1). In the absence of CT interactions between the ET and  $\text{I}_3$  species, all carriers (spins) should be confined within the conducting ET ( $\text{C}_{10}\text{H}_8\text{S}_8$ ) sheets, and no hyperfine structures are expected. Owing to the H bonding shown in Figure 1c, all four terminal I atoms in the two crystallographically independent  $\text{I}_3^-$  species are inequivalent in the hyperfine interactions. Consequently, a single peak is divided into many fine peaks.

### 3.5. Chemistry Driving the Massless–Massive Fermion Transformation

The occurrence and disappearance of Dirac (massless) fermions in the standard (massive) fermion systems discussed above revealed the importance of a chemical equilibrium in the D– $\text{I}_3$  interaction. This is a spontaneous solid-state redox reaction described by the following formula,



$$K = \frac{[D^{(0.5-\delta)+}][I_3^{(1-\delta)-}]}{[D^{(0.5-\varepsilon)+}][I_3^{(1-\varepsilon)-}]} \quad (\varepsilon \neq \delta, \quad D = \text{ET, STF, and BETS}) \quad (2)$$

As the equilibrium constants ( $K$  in Equation (2)) generally depend on the temperature, the redox reaction (Equation (1)) proceeds depending on the temperature. Similarly, the chemical potentials generally depend on both thermodynamic conditions and chemical environments when intermolecular interactions are important, such as those in solid states. Still, the reaction described by Equations (1) and (2) in  $\alpha$ -D<sub>2</sub>I<sub>3</sub> is unusual in that  $\varepsilon$  and  $\delta$  can take any non-integer number, respectively, resulting in continuous change in the (metastable) oxidation states of all the chemical species involved in the reaction (Supplementary Figure S2). This is only possible when both D and I<sub>3</sub> species form energy bands based on close D–D and D–I<sub>3</sub> interactions. When the temperature changes, a slight change in the electron density distribution in the unit cell of  $\alpha$ -D<sub>2</sub>I<sub>3</sub> caused by the reaction (Equation (1)) drives band deformation as shown in Figures 3 and 4. With decreasing temperature (296 K → 150 K in the ET salt and 296 K → 80 K in the BETS salt), more and more electrons or holes (massive fermions) travel to the Dirac points, because the energy at the developing Dirac points continuously becomes lower and lower until it is finally lowest in the respective bands. Thus, in a wide temperature range, a part of the doped electrons/holes from the I<sub>3</sub> anions (massive fermions) collaborate with the thermally activated electrons/holes at the Dirac points (massless fermions) in the electronic properties. Accordingly, the transformation between massless and massive fermions can occur in a continuous manner. In summary, the abovementioned unusual chemical situation drives a continuous but qualitative change in the electrical conductivity, magnetic susceptibility, dimensionality in the electronic system, and the direction of electron transfer (electron- or hole-doping from the I<sub>3</sub> species), in addition to the effective mass of the fermions by temperature variation.

#### 4. Conclusions

The band reshaping of  $\alpha$ -D<sub>2</sub>I<sub>3</sub> (D = ET, BETS) under ambient pressure with respect to  $T$  demonstrates the lifecycle of DF, i.e., the entire process of their occurrence, development, and disappearance. Massless and massive fermions coexist and crossover each other via band reshaping. The D–I<sub>3</sub> CT interactions play key roles in  $T$ -sensitive band reshaping. As the organic DF systems share many features with other types of DF systems, these findings shed new light on the entirety of DF systems and accelerate the progression of related studies. However, the electronic properties specific to DFs, such as  $T$  dependencies of the electrical resistivity and magnetic susceptibility and wavenumber dependence of the optical conductivity, are often featureless when compared with those of SFs [1–36]. Such monotonical behaviors of the electronic properties could be explained in various ways. As the analyses of the calculation and experimental results in this study were based on assumption and approximation as in other studies, further research from different perspectives and methods for crosschecking are required for a deeper insight into the nature of DFs.

**Supplementary Materials:** The following supporting information can be downloaded at: <https://www.mdpi.com/article/10.3390/magnetochemistry9060153/s1>, Scheme S1: Syntheses of neutral BETS and STF; Figure S1: Microwave-power ( $P$ ) dependencies of ESR spectra of  $\alpha$ -ET<sub>2</sub>I<sub>3</sub> (single crystal,  $B // a$ -axis) at 296 K; Figure S2: Temperature dependence of the molecular (Bader) charges on the crystallographically independent D (A, A', B, and C) and I<sub>3</sub> (1 and 2) species in (a)  $\alpha$ -ET<sub>2</sub>I<sub>3</sub> and (b)  $\alpha$ -BETS<sub>2</sub>I<sub>3</sub>.

**Author Contributions:** R.O. measured the resistivity and ESR spectra; R.O. and T.N. analyzed the resistivity, magnetic susceptibility, and ESR data; I.Y. and T.S. measured the magnetic susceptibility and calculated the band structures; K.O. and K.K. assisted R.O. in measuring the ESR spectra and resistivity, respectively; T.N., I.Y. and T.S. drafted the manuscript. All authors have read and agreed to the published version of the manuscript.

**Funding:** This work was partially funded by a Grant-in-Aid for Challenging Exploratory Research (18K19061) and a Grant-in-Aid for Scientific Research (B) (22H02034) of JSPS, the Iketani Science and Technology Foundation (ISTF; 0331005-A), the Research Grant Program of the Futaba Foundation, the CASIO Science Promotion Foundation, an Ehime University Grant for Project for the Promotion of Industry/University Cooperation, and the Canon Foundation (Science and Technology that Achieve a Good Future).

**Institutional Review Board Statement:** Not applicable.

**Informed Consent Statement:** Not applicable.

**Data Availability Statement:** The relevant data supporting our key findings are available within the article and the Supplementary Information file. All raw data generated during our current study are available from the corresponding authors upon reasonable request, which should be addressed to T. Naito.

**Acknowledgments:** The authors are grateful to H. Sawa (Nagoya University) for providing a part of the atomic coordinates of  $\alpha$ -D<sub>2</sub>I<sub>3</sub>. We would like to acknowledge the assistance provided by S. Mori and R. Konishi (ADRES, Ehime University) in the X-ray structural analyses. We would also like to thank R. Nakamura for partly conducting the resistivity measurements with the help of T. Yamamoto (Ehime University). The computational resources were provided by ISSP, University of Tokyo supercomputer (Projects: 2022-Ba-0061 and 2021-Ba-0028) and the Research Center for Computational Science, Okazaki, Japan (Projects: 21-IMS-C088 and 22-IMS-C088).

**Conflicts of Interest:** The authors declare no conflict of interest.

## References

1. Castro Neto, A.H.; Guinea, F.; Peres, N.M.R.; Novoselov, K.S.; Geim, A.K. The electronic properties of graphene. *Rev. Mod. Phys.* **2009**, *81*, 109–162. [[CrossRef](#)]
2. Park, S.H.; Sammon, M.; Mele, E.; Low, T. Plasmonic gain in current biased tilted Dirac nodes. *Nat. Commun.* **2022**, *13*, 7667. [[CrossRef](#)] [[PubMed](#)]
3. Geng, D.; Zhou, H.; Yue, S.; Sun, Z.; Cheng, P.; Chen, L.; Meng, S.; Wu, K.; Feng, B. Observation of gapped Dirac cones in a two-dimensional Su-Schrieffer-Heeger lattice. *Nat. Commun.* **2022**, *13*, 7000. [[CrossRef](#)] [[PubMed](#)]
4. Lu, Q.; Cook, J.; Zhang, X.; Chen, K.Y.; Snyder, M.; Nguyen, D.T.; Sreenivasa Reddy, P.V.; Qin, B.; Zhan, S.; Zhao, L.-D.; et al. Realization of unpinned two-dimensional dirac states in antimony atomic layers. *Nat. Commun.* **2022**, *13*, 4603. [[CrossRef](#)]
5. Bauernfeind, M.; Erhardt, J.; Eck, P.; Thakur, P.K.; Gabel, J.; Lee, T.-L.; Schäfer, J.; Moser, S.; Di Sante, D.; Claessen, R.; et al. Design and realization of topological Dirac fermions on a triangular lattice. *Nat. Commun.* **2021**, *12*, 5396. [[CrossRef](#)] [[PubMed](#)]
6. Guo, C.; Alexandradinata, A.; Putzke, C.; Estry, A.; Tu, T.; Kumar, N.; Fan, F.-R.; Zhang, S.; Wu, Q.; Yazyev, O.V.; et al. Temperature dependence of quantum oscillations from non-parabolic dispersions. *Nat. Commun.* **2021**, *12*, 6213. [[CrossRef](#)]
7. Park, H.; Gao, W.; Zhang, X.; Oh, S.S. Nodal lines in momentum space: Topological invariants and recent realizations in photonic and other systems. *Nanophotonics* **2022**, *11*, 2779–2801. [[CrossRef](#)]
8. Bai, Y.; Li, N.; Li, R.; Liu, P. Ultrafast dynamics of helical Dirac fermions in the topological insulators. *Adv. Physics: X* **2022**, *7*, 2013134. [[CrossRef](#)]
9. Jana, S.; Bandyopadhyay, A.; Datta, S.; Bhattacharya, D.; Jana, D. Emerging properties of carbon based 2D material beyond graphene. *J. Phys.: Cond. Mat.* **2022**, *34*, 053001. [[CrossRef](#)]
10. Yilmatz, T.; Tong, X.; Dai, Z.; Sadowski, J.T.; Schwier, E.F.; Shimada, K.; Hwang, S.; Kisslinger, K.; Kaznatcheev, K.; Vescovo, E.; et al. Emergent flat band electronic structure in a VSe<sub>2</sub>/Bi<sub>2</sub>Se<sub>3</sub> heterostructure. *Commun. Mater.* **2021**, *2*, 11. [[CrossRef](#)]
11. Khoury, J.F.; Schoop, L.M. Chemical bonds in topological materials. *Trends Chem.* **2021**, *3*, 700–715. [[CrossRef](#)]
12. Kumar, N.; Guin, S.N.; Manna, K.; Shekhar, C.; Felser, C. Topological quantum materials from the viewpoint of chemistry. *Chem. Rev.* **2021**, *121*, 2780–2815. [[CrossRef](#)] [[PubMed](#)]
13. Bhattacharyya, S.; Akhgar, G.; Gebert, M.; Karel, J.; Edmonds, M.T.; Fuhrer, M.S. Recent progress in proximity coupling of magnetism to topological insulators. *Adv. Mater.* **2021**, *33*, 2007795. [[CrossRef](#)] [[PubMed](#)]
14. Mandal, I.; Saha, K. Thermopower in an anisotropic two-dimensional Weyl semimetal. *Phys. Rev. B* **2020**, *101*, 045101. [[CrossRef](#)]
15. Neubauer, D.; Yaresko, A.; Li, W.; Löhle, A.; Hübner, R.; Schilling, M.B.; Shekhar, C.; Felser, C.; Dressel, M.; Pronin, A.V. Optical conductivity of the Weyl semimetal NbP. *Phys. Rev. B* **2018**, *98*, 195203. [[CrossRef](#)]
16. Chen, Z.-G.; Shi, Z.; Yang, W.; Lu, X.; Lai, Y.; Yan, H.; Wang, F.; Zhang, G.; Li, Z. Observation of an intrinsic bandgap and Landau level renormalization in graphene/boron-nitride heterostructures. *Nat. Commun.* **2014**, *5*, 4461. [[CrossRef](#)]
17. Timusk, T.; Carbotte, J.P.; Homes, C.C.; Basov, D.N.; Sharapov, S.G. Three-dimensional Dirac fermions in quasicrystals as seen via optical conductivity. *Phys. Rev. B* **2013**, *87*, 235121. [[CrossRef](#)]

18. Pop, F.; Mézière, C.; Allain, M.; Auban-Senzier, P.; Tajima, N.; Hirobe, D.; Yamamoto, H.M.; Canadell, E.; Avarvari, N. Unusual stoichiometry, band structure and band filling in conducting enantiopure radical cation salts of TM-BEDT-TTF showing helical packing of the donors. *J. Mater. Chem. C* **2021**, *9*, 10777–10786. [[CrossRef](#)]
19. Hirata, M.; Kobayashi, A.; Berthier, C.; Kanoda, K. Interacting chiral electrons at the 2D Dirac points: A review. *Rep. Prog. Phys.* **2021**, *84*, 036502. [[CrossRef](#)]
20. Kajita, K.; Nishio, Y.; Tajima, N.; Suzumura, Y.; Kobayashi, A. Molecular Dirac fermion systems –Theoretical and experimental approaches –. *J. Phys. Soc. Jpn.* **2014**, *83*, 072002. [[CrossRef](#)]
21. Naito, T.; Doi, R.; Suzumura, Y. Exotic Dirac cones on the band structure of  $\alpha$ -STF<sub>2</sub>I<sub>3</sub> at ambient temperature and pressure. *J. Phys. Soc. Jpn.* **2020**, *89*, 023701. [[CrossRef](#)]
22. Nomoto, T.; Imajo, S.; Akutsu, H.; Nakazawa, Y.; Kohama, Y. Correlation-driven organic 3D topological insulator with relativistic fermions. *Nat. Commun.* **2023**, *14*, 2130. [[CrossRef](#)] [[PubMed](#)]
23. Kawasugi, Y.; Masuda, H.; Uebe, M.; Yamamoto, H.M.; Kato, R.; Nishio, Y.; Tajima, N. Pressure-induced phase switching of Shubnikov-de Haas oscillations in the molecular Dirac fermion system  $\alpha$ -(BETS)<sub>2</sub>I<sub>3</sub>. *Phys. Rev. B* **2021**, *103*, 205140. [[CrossRef](#)]
24. Tsumuraya, T.; Suzumura, Y. First-principles study of the effective Hamiltonian for Dirac fermions with spin-orbit coupling in two-dimensional molecular conductor  $\alpha$ -(BETS)<sub>2</sub>I<sub>3</sub>. *Eur. Phys. J. B* **2021**, *94*, 17. [[CrossRef](#)]
25. Kitou, S.; Tsumuraya, T.; Sawahata, H.; Ishii, F.; Hiraki, K.-I.; Nakamura, T.; Katayama, N.; Sawa, H. Ambient-pressure Dirac electron system in the quasi-two-dimensional molecular conductor  $\alpha$ -(BETS)<sub>2</sub>I<sub>3</sub>. *Phys. Rev. B* **2021**, *103*, 035135. [[CrossRef](#)]
26. Naito, T.; Doi, R. Band structure and physical properties of  $\alpha$ -STF<sub>2</sub>I<sub>3</sub>: Dirac electrons in disordered conduction sheets. *Crystals* **2020**, *10*, 270. [[CrossRef](#)]
27. Ohki, D.; Yoshimi, K.; Kobayashi, A. Transport properties of the organic Dirac electron system  $\alpha$ -(BEDT-TSeF)<sub>2</sub>I<sub>3</sub>. *Phys. Rev. B* **2020**, *102*, 235116. [[CrossRef](#)]
28. Uykur, E.; Li, W.; Kuntscher, C.A.; Dressel, M. Optical signatures of energy gap in correlated Dirac fermions. *npj Quantum Mater.* **2019**, *4*, 19. [[CrossRef](#)]
29. Hirata, M.; Ishikawa, K.; Matsuno, G.; Kobayashi, A.; Miyagawa, K.; Tamura, M.; Berthier, C.; Kanoda, K. Anomalous spin correlations and excitonic instability of interacting 2D Weyl fermions. *Science* **2017**, *358*, 1403–1406. [[CrossRef](#)]
30. Beyer, R.; Dengl, A.; Peterseim, T.; Wackerow, S.; Ivek, T.; Pronin, A.V.; Schweitzer, D.; Dressel, M. Pressure-dependent optical investigations of  $\alpha$ -(BEDT-TTF)<sub>2</sub>I<sub>3</sub>: Tuning charge order and narrow gap towards a Dirac semimetal. *Phys. Rev. B* **2016**, *93*, 195116. [[CrossRef](#)]
31. Hirata, M.; Ishikawa, K.; Miyagawa, K.; Tamura, M.; Berthier, C.; Basko, D.; Kobayashi, A.; Matsuno, G.; Kanoda, K. Observation of an anisotropic Dirac cone reshaping and ferrimagnetic spin polarization in an organic conductor. *Nat. Commun.* **2016**, *7*, 12666. [[CrossRef](#)] [[PubMed](#)]
32. Liu, D.; Ishikawa, K.; Takehara, R.; Miyagawa, K.; Tamura, M.; Kanoda, K. Insulating nature of strongly correlated massless Dirac fermions in an organic crystal. *Phys. Rev. Lett.* **2016**, *116*, 226401. [[CrossRef](#)] [[PubMed](#)]
33. Ogata, M.; Ozaki, S.; Matsuura, H. Anomalous Spin Transport Properties of Gapped Dirac Electrons with Tilting. *J. Phys. Soc. Jpn.* **2022**, *91*, 023708. [[CrossRef](#)]
34. Suzumura, Y.; Tsumuraya, T. Electric and magnetic responses of two-dimensional Dirac electrons in organic conductor  $\alpha$ -(BETS)<sub>2</sub>I<sub>3</sub>. *J. Phys. Soc. Jpn.* **2021**, *90*, 124707. [[CrossRef](#)]
35. Morinari, T.; Suzumura, Y. On the possible zero-gap state in organic conductor  $\alpha$ -(BEDT-TSF)<sub>2</sub>I<sub>3</sub> under pressure. *J. Phys. Soc. Jpn.* **2014**, *83*, 094701. [[CrossRef](#)]
36. Suzumura, Y.; Naito, T. Conductivity of two-dimensional Dirac electrons close to merging in organic conductor  $\alpha$ -STF<sub>2</sub>I<sub>3</sub> at ambient pressure. *J. Phys. Soc. Jpn.* **2022**, *91*, 064701. [[CrossRef](#)]
37. Oroszlány, L.; Dóra, B.; Cserti, J.; Cortijo, A. Topological and trivial magnetic oscillations in nodal loop semimetals. *Phys. Rev. B* **2018**, *97*, 205107. [[CrossRef](#)]
38. Feilhauer, J.; Apel, W.; Schweitzer, L. Merging of the Dirac points in electronic artificial graphene. *Phys. Rev. B* **2015**, *92*, 245424. [[CrossRef](#)]
39. Delplace, P.; Gómez-León, A.; Platero, G. Merging of Dirac points and Floquet topological transitions in ac-driven graphene. *Phys. Rev. B* **2013**, *88*, 245422. [[CrossRef](#)]
40. Dóra, B.; Herbut, I.F.; Moessner, R. Coupling, merging, and splitting Dirac points by electron-electron interaction. *Phys. Rev. B* **2013**, *88*, 075126. [[CrossRef](#)]
41. Wang, L.; Fu, L. Interaction-induced merging of Dirac points in non-Abelian optical lattices. *Phys. Rev. A* **2013**, *87*, 053612. [[CrossRef](#)]
42. Tarruell, L.; Greif, D.; Uehlinger, T.; Jotzu, G.; Esslinger, T. Creating, moving and merging Dirac points with a Fermi gas in a tunable honeycomb lattice. *Nature* **2012**, *483*, 302–305. [[CrossRef](#)] [[PubMed](#)]
43. Montambaux, G.; Piéchon, F.; Fuchs, J.-N.; Goerbig, M.O. A universal Hamiltonian for motion and merging of Dirac points in a two-dimensional crystal. *Eur. Phys. J. B* **2009**, *72*, 509–520. [[CrossRef](#)]
44. Pereira, V.M.; Castro Neto, A.H.; Peres, N.M.R. Tight-binding approach to uniaxial strain in graphene. *Phys. Rev. B* **2009**, *80*, 045401. [[CrossRef](#)]

45. Naito, T.; Kobayashi, H.; Kobayashi, A. The electrical behavior of charge-transfer salts based on an unsymmetrical donor bis(ethylenedithio)diselenadithiafulvalene (STF): Disorder effect on the transport properties. *Bull. Chem. Soc. Jpn.* **1997**, *70*, 107–114. [[CrossRef](#)]
46. Inokuchi, M.; Tajima, H.; Kobayashi, A.; Ohta, T.; Kuroda, H.; Kato, R.; Naito, T.; Kobayashi, H. Electrical and optical properties of  $\alpha$ -(BETS)<sub>2</sub>I<sub>3</sub> and  $\alpha$ -(BEDT-STF)<sub>2</sub>I<sub>3</sub>. *Bull. Chem. Soc. Jpn.* **1995**, *68*, 547–553. [[CrossRef](#)]
47. Kato, R.; Kobayashi, H.; Kobayashi, A. Synthesis and properties of bis(ethylenedithio)tetraselenafulvalene (BEDT-TSeF) compounds. *Synth. Met.* **1991**, *42*, 2093–2096. [[CrossRef](#)]
48. Bender, K.; Hennig, I.; Schweitzer, D.; Dietz, K.; Endres, H.; Keller, H.J. Synthesis, structure and physical properties of a two-dimensional organic metal, di[bis(ethylenedithio)tetrathiofulvalene]triiodide, (BEDT-TTF)<sub>2</sub><sup>+</sup>I<sub>3</sub><sup>-</sup>. *Mol. Cryst. Liq. Cryst.* **1984**, *108*, 359–371. [[CrossRef](#)]
49. Kakiuchi, T.; Wakabayashi, Y.; Sawa, H.; Takahashi, T.; Nakamura, T. Charge ordering in  $\alpha$ -(BEDT-TTF)<sub>2</sub>I<sub>3</sub> by synchrotron X-ray diffraction. *J. Phys. Soc. Jpn.* **2007**, *76*, 113702. [[CrossRef](#)]
50. Rothaemel, B.; Forró, L.; Cooper, J.R.; Schilling, J.S.; Weger, M.; Bele, P.; Brunner, H.; Schweitzer, D.; Keller, H.J. Magnetic susceptibility of  $\alpha$  and  $\beta$  phases of di[bis(ethylenedithio)tetrathiafulvalene]tri-iodide [(BEDT-TTF)<sub>2</sub>I<sub>3</sub>] under pressure. *Phys. Rev. B* **1986**, *34*, 704–712. [[CrossRef](#)]
51. Tajima, N.; Tamura, M.; Nishio, Y.; Kajita, K.; Iye, Y. Transport property of an organic conductor  $\alpha$ -(BEDT-TTF)<sub>2</sub>I<sub>3</sub> under high pressure—Discovery of a novel type of conductor. *J. Phys. Soc. Jpn.* **2000**, *69*, 543–551. [[CrossRef](#)]
52. Ivek, T.; Korin-Hamzić, B.; Milat, O.; Tomić, S.; Clauss, C.; Drichko, N.; Schweitzer, D.; Dressel, M. Electrodynamic response of the charge ordering phase: Dielectric and optical studies of  $\alpha$ -(BEDT-TTF)<sub>2</sub>I<sub>3</sub>. *Phys. Rev. B* **2011**, *83*, 165128. [[CrossRef](#)]
53. Venturini, E.L.; Azevedo, L.J.; Schirber, J.E.; Williams, J.M.; Wang, H.H. ESR study of two phases of di[bis(ethylenedithio)tetrathiafulvalene]triiodide [(BEDT-TTF)<sub>2</sub>I<sub>3</sub>]. *Phys. Rev. B* **1985**, *32*, 2819–2823. [[CrossRef](#)] [[PubMed](#)]
54. Sugano, T.; Saito, G.; Kinoshita, M. Conduction-electron-spin resonance in organic conductors:  $\alpha$  and  $\beta$  phases di[bis(ethylenedithio)tetrathiafulvalene]triiodide [(BEDT-TTF)<sub>2</sub>I<sub>3</sub>]. *Phys. Rev. B* **1986**, *34*, 117–125. [[CrossRef](#)] [[PubMed](#)]
55. Uji, S.; Kodama, K.; Sugii, K.; Takahide, Y.; Terashima, T.; Kurita, N.; Tsuchiya, S.; Kohno, M.; Kimata, M.; Yamamoto, K.; et al. Kosterlitz-Thouless-type transition in a charge ordered state of the layered organic conductor  $\alpha$ -(BEDT-TTF)<sub>2</sub>I<sub>3</sub>. *Phys. Rev. Lett.* **2013**, *110*, 196602. [[CrossRef](#)] [[PubMed](#)]
56. Seo, H. Charge ordering in organic ET compounds. *J. Phys. Soc. Jpn.* **2000**, *69*, 805–820. [[CrossRef](#)]
57. Seo, H.; Merino, J.; Yoshioka, H.; Ogata, M. Theoretical aspects of charge ordering in molecular conductors. *J. Phys. Soc. Jpn.* **2006**, *75*, 051009. [[CrossRef](#)]
58. Takano, Y.; Hiraki, K.; Yamamoto, H.M.; Nakamura, T.; Takahashi, T. Charge disproportionation in the organic conductor,  $\alpha$ -(BEDT-TTF)<sub>2</sub>I<sub>3</sub>. *J. Phys. Chem. Solids* **2001**, *62*, 393–395. [[CrossRef](#)]
59. Yamamoto, K.; Kowalska, A.A.; Yakushi, K. Direct observation of ferroelectric domains created by Wigner crystallization of electrons in  $\alpha$ -[Bis(ethylenedithio)tetrathiafulvalene]<sub>2</sub>I<sub>3</sub>. *Appl. Phys. Lett.* **2010**, *96*, 122901. [[CrossRef](#)]
60. Kondo, R.; Kagoshima, S. Crystal and electronic structures of  $\alpha$ -(BEDT-TTF)<sub>2</sub>I<sub>3</sub> under uniaxial strains. *J. Phys. IV France* **2004**, *114*, 523–525. [[CrossRef](#)]
61. Kondo, R.; Kagoshima, S.; Harada, J. Crystal structure analysis under uniaxial strain at low temperature using a unique design of four-axis x-ray diffractometer with a fixed sample. *Rev. Sci. Instrum.* **2005**, *76*, 093902. [[CrossRef](#)]
62. Ishibashi, S.; Tamura, T.; Kohyama, M.; Terakura, K. *Ab initio* electronic-structure calculations for  $\alpha$ -(BEDT-TTF)<sub>2</sub>I<sub>3</sub>. *J. Phys. Soc. Jpn.* **2006**, *75*, 015005. [[CrossRef](#)]
63. Naito, T.; Suzumura, Y. Theoretical model for novel electronic state in a Dirac electron system close to merging: An imaginary element between sulfur and selenium. *Crystals* **2022**, *12*, 346. [[CrossRef](#)]
64. Kino, H.; Miyazaki, T. First-Principles Study of Electronic Structure in  $\alpha$ -(BEDT-TTF)<sub>2</sub>I<sub>3</sub> at Ambient Pressure and with Uniaxial Strain. *J. Phys. Soc. Jpn.* **2006**, *75*, 034704. [[CrossRef](#)]
65. Monteverde, M.; Goerbig, M.O.; Auban-Senzier, P.; Navarin, F.; Henck, H.; Pasquier, C.R.; Mézière, C.; Batail, P. Coexistence of Dirac and massive carriers in  $\alpha$ -(BEDT-TTF)<sub>2</sub>I<sub>3</sub> under hydrostatic pressure. *Phys. Rev. B* **2013**, *87*, 245110. [[CrossRef](#)]
66. Katayama, S.; Kobayashi, A.; Suzumura, Y. Pressure-induced zero-gap semiconducting state in organic conductor  $\alpha$ -(BEDT-TTF)<sub>2</sub>I<sub>3</sub> salt. *J. Phys. Soc. Jpn.* **2006**, *75*, 054705. [[CrossRef](#)]
67. Naito, T.; Inabe, T. Molecular hexagonal perovskite: A new type of organic–inorganic hybrid conductor. *J. Solid State Chem.* **2003**, *176*, 243–249. [[CrossRef](#)]
68. Naito, T.; Matsuo, S.; Inabe, T.; Toda, Y. Carrier dynamics in a series of organic magnetic superconductors. *J. Phys. Chem. C* **2012**, *116*, 2588–2593. [[CrossRef](#)]
69. Dolomanov, O.V.; Bourhis, L.J.; Gildea, R.J.; Howard, J.A.K.; Puschmann, H. OLEX2: A complete structure solution, refinement and analysis program. *J. Appl. Cryst.* **2009**, *42*, 339–341. [[CrossRef](#)]
70. Kresse, G.; Hafner, J. *Ab initio* molecular dynamics for liquid metals. *Phys. Rev. B* **1993**, *47*, 558–561. [[CrossRef](#)]
71. Mochalin, V.N.; Shenderova, O.; Ho, D.; Gogotsi, Y. The properties and applications of nanodiamonds. *Nat. Nanotechnol.* **2012**, *7*, 11–23. [[CrossRef](#)] [[PubMed](#)]
72. Pouget, J.-P.; Alemany, P.; Canadell, E. Donor-anion interactions in quarter-filled low-dimensional organic conductors. *Mater. Horiz.* **2018**, *5*, 590–640. [[CrossRef](#)]

73. Alemany, P.; Pouget, J.-P.; Canadell, E. Essential role of anions in the charge ordering transition of  $a$ -(BEDT-TTF) $_2$ I $_3$ . *Phys. Rev. B* **2012**, *85*, 195118. [[CrossRef](#)]
74. Ivek, T.; Čulo, M.; Kuveždić, M.; Tutiš, E.; Basletić, M.; Mihaljević, B.; Tafra, E.; Tomić, S.; Löhle, A.; Dressel, M.; et al. Semimetallic and charge-ordered  $a$ -(BEDT-TTF) $_2$ I $_3$ : On the role of disorder in dc transport and dielectric properties. *Phys. Rev. B* **2017**, *96*, 075141. [[CrossRef](#)]
75. Kim, A.S.; Walter, A.L.; Moreschini, L.; Seyller, T.; Horn, K.; Rotenberg, E.; Bostwick, A. Coexisting massive and massless Dirac fermions in symmetry-broken bilayer graphene. *Nat. Mater.* **2013**, *12*, 887–892. [[CrossRef](#)]
76. Zhou, B.; Dong, S.; Wang, X.; Zhang, K. Prediction of two-dimensional  $d$ -block elemental materials with normal honeycomb, triangular-dodecagonal, and square-octagonal structures from first principles. *Appl. Surf. Sci.* **2017**, *419*, 484–496. [[CrossRef](#)]
77. Yuan, X.; Yan, Z.; Song, C.; Zhang, M.; Li, Z.; Zhang, C.; Liu, Y.; Wang, W.; Zhao, M.; Lin, Z.; et al. Chiral Landau levels in Weyl semimetal NbAs with multiple topological carriers. *Nat. Commun.* **2018**, *9*, 1854. [[CrossRef](#)]
78. Luyang, W.; Dao-Xin, Y. Coexistence of spin-1 fermion and Dirac fermion on the triangular kagome lattice. *Phys. Rev. B* **2018**, *98*, 161403. [[CrossRef](#)]
79. Miyazaki, T.; Kino, H. Atomic and electronic structures of the high-pressure superconductor  $b'$ -(BEDT-TTF) $_2$ ICl $_2$ : A first-principles study of the pressure effects. *Phys. Rev. B* **2003**, *68*, 220511. [[CrossRef](#)]
80. Miyazaki, T.; Kino, H. First-principles study of the pressure effects on  $b'$ -(BEDT-TTF) $_2$ AuCl $_2$ . *Phys. Rev. B* **2006**, *73*, 035107. [[CrossRef](#)]
81. Fujiyama, S.; Maebashi, H.; Tajima, N.; Tsumuraya, T.; Cui, H.-B.; Ogata, M.; Kato, R. Large diamagnetism and electromagnetic duality in two-dimensional Dirac electron system. *Phys. Rev. Lett.* **2022**, *128*, 027201. [[CrossRef](#)] [[PubMed](#)]
82. Coulon, C.; Clérac, R. Electron spin resonance: A major probe for molecular conductors. *Chem. Rev.* **2004**, *104*, 5655–5687. [[CrossRef](#)] [[PubMed](#)]

**Disclaimer/Publisher's Note:** The statements, opinions and data contained in all publications are solely those of the individual author(s) and contributor(s) and not of MDPI and/or the editor(s). MDPI and/or the editor(s) disclaim responsibility for any injury to people or property resulting from any ideas, methods, instructions or products referred to in the content.